RSC Advances

ROYAL SOCIETY OF CHEMISTRY

www.rsc.org/advances

Electrochemical capacitance of carbon quantum dots-polypyrrole/titania nanotube hybrid

Yibing Xie [a, b*], **Hongxiu Du** [a, b]

Carbon quantum dots modified polypyrrole/titania (CQDs-PPy/TiO_2) nanotube hybrid was designed as supercapacitor electrode material for an energy storage. CQDs-PPy/TiO_2 was prepared by incorporating CQDs-hybridized PPy into well-aligned titania nanotube array. CQDs-PPy/TiO_2 exhibited a highly-ordered heterogeneous coaxial nanotube structure. CQDs hybridizing modification could well improve the electrical conductivity of PPy. The charge transfer resistance decreased from 22.4 mΩ cm^{-2} to 9.3 mΩ cm^{-2} and the ohmic resistance decreased from 0.817 for to 0.154 Ω cm^{-2} when PPy/TiO_2 was converted into CQDs-PPy/TiO_2 nanotube hybrid. The specific capacitance was accordingly enhanced from 482 F g^{-1} (or 161 mF cm^{-2}) for PPy/TiO_2 to 849 F g^{-1} (or 212 mF cm^{-2}) for CQDs-PPy/TiO_2 at a current density of 0.5 A g^{-1}. The capacitance retention was slightly increased from 78.5% to 89.3% after 2000 cycles at high current density of 20 A g^{-1}. The effective incorporation CQDs into PPy could simultaneously increase electrochemical capacitance and cycle stability of PPy, leading to a superior electrochemical performance. A flexible solid-state supercapacitor based on CQDs-PPy nanohybrid exhibited the stable capacitive performance at both planar and bending state. CQDs-hybridized PPy presented the promising application as supercapacitor electrode material for energy storage.

1. Introduction

Nowadays, conducting polymers have been widely explored for highly performanced pseudocapacitors because of its excellent energy storage capacity, low cost, high availability and environmental friendliness [1-6]. Polypyrrole (PPy) has the unique π-conjugated system and can provide an effective route for the flow of electronic charges [7]. PPy has been extensively studied for

[a] School of Chemistry and Chemical Engineering, Southeast University, Nanjing 211189, China, E-mail: ybxie@seu.edu.cn

[b] Suzhou Research Institute of Southeast University, Suzhou 215123, China

electrochemical energy storage application [8, 9]. The microstructure of PPy is the crucial issue to determine its electrochemical performance [10]. Normally, nanostructured electrode materials generally exhibit superior properties compared to their bulk counterparts, owing to their larger surface area and shorter charge transfer pathway [11, 12]. The well-aligned titania (TiO_2) nanotube array has been explored as the support of electrodes thanks to high surface area and chemical/electrochemical stability [13]. The highly ordered TiO_2 nanotube array with the controlled morphologies can be well prepared by an electrochemical anodization method [14, 15]. The hybrid of PPy and TiO_2 with well-designed nanostructure and high surface area can be regarded as suitable electrode material of electrochemical supercapacitors [16]. However, the main drawback using PPy as supercapacitor electrode is mainly due to its inherent low electrical conductivity and poor stability during cycling process [17]. Several approaches have been proposed to overcome these shortcomes, which includes using the substrate of titanium nitride to improve conductivity [5, 18-21] and adding conductive nanoparticles to improve the rate of electron transport [22-26]. Patil et al. have reported the formation of polypyrrole/polyacrylic acid/silver composite electrode by chemical polymerization via a simple and cost effective dip coating technique [27]. Dhibar et al. have fabricated a silver-polyaniline/multiwalled carbon nanotubes nanocomposite by a low-cost and simple process [28]. Wei et al. have directly deposited polypyrrole-silver composites on nickel foam via the redox reaction between pyrrole and silver nitrate [29]. A synergistic effect between PPy and conductive nanoparticles has been presumed upon to enhance the mechanical and conducting properties. Commonly, carbon nanomaterials such as carbon quantum dots, carbon nanotubes and graphene have attracted great interest due to high conductivity, long cycle life and good cycling stability for supercapacitor applications [30-32]. However, the drawback of low capacitance still needs to be overcome. The overall aim of this work is thus to develop conductive hybrid material to improve supercapacitance performance and cycling stability of PPy. Water-soluble CQDs was used to directly incorporate into bulk PPy to form highly conducitive CQDs-PPy composite film during the electropolymerization process.

In this study, CQDs-PPy/TiO_2 nanotube hybrid were synthesized by incorporating CQDs-hybridized PPy into TiO_2 nanotube array using electrochemical polymerization method. Highly conductive CQDs were used to improve electrical conductivity and electroactivity of PPy. TiO_2 nanotube hybrid as an electrode substrate was used to improve the utilization of PPy.Hence, CQDs-PPy/TiO_2 nanotube hybrid is expected to exhibit superior capacitance performance and high cycling stability as well.

2. Experimental

2.1 Materials

Titanium sheet (Ti, purity > 99.6%, thickness 0.2 mm) was purchased from Good fellow Cambridge Ltd. Pyrrole monomer (Py, chemically pure, purity > 98%), carbon rod (C, spectrum pure, purity > 99.9%). Other chemicals used were of analytical grade without any further treatment. All aqueous solutions were prepared with double-distilled water.

2.2 Synthesis of CQDs-PPy/TiO_2 nanotube hybrid

CQDs-PPy/TiO_2 nanotube hybrid was synthesized using TiO_2 nanotube array as an electrode substrate. Firstly, TiO_2 nanotube array was directly formed on Ti sheet by an anodization process which was conducted at 30 V for 2 h in water and ethylene glycol mixture solution (volume ratio, 50/50) containing 0.2 M ammonium fluoride and 0.5 M phosphoric acid. An annealing treatment at 450 °C for 2 h was conducted to form anatase TiO_2 nanotube array. Then, a normal pulse voltammetry deposition method was adopted to synthetize CQDs-PPy/TiO_2 nanotube hybrid in a three-electrode system using TiO_2 nanotube array as a working electrode, Pt as a counter electrode and Hg/Hg_2Cl_2 as a reference electrode. The aqueous reaction solution contained 0.001 M carbon quantum dots, 0.15 M pyrrole monomer and 0.1 M lithium perchlorate ($LiClO_4$) supporting electrolyte. PPy/TiO_2 nanotube hybrid was also prepared in the same aqueous solution as above without carbon quantum dots. The pulse potential was increased from 0.7 to 1.1 V with a pulse potential increment of 0.001 V. The pulse width was 0.06 s and the pulse period was 4 s. As-formed

CQDs-PPy/TiO_2 and PPy/TiO_2 nanotube hybrid was repeatedly washed with double-distilled water and finally dried at room temperature. Flexible supercapacitor application was investigated using CQDs-PPy nanohybrid as freestanding film electrode. Flexible solid-state supercapacitor was constructed using CQDs-PPy nanohybrid film as freestanding film electrode. Firstly, CQDs-PPy nanohybrid film was fabricated by dissolving TiO_2 template from CQDs-PPy/TiO_2 nanotube hybrid in 2.0 M hydrofluoric acid aqueous solution. PVA/H_2SO_4 gel electrolyte was prepared according to the previously reported method [3]. CQDs-PPy nanohybrid film electrode was fabricated by spreading two pieces of CQDs-PPy nanohybrid films on both sides of porous dialysis membrane. Herein, porous dialysis membrane was initially saturated with PVA/H_2SO_4 gel electrolyte. Flexible solid-state supercapacitor was assembled by wrapping CQDs-PPy nanohybrid film electrode using polyethylene terephthalate (PET) film, and connecting CQDs-PPy nanohybrid film electrode using copper wires.

2.3 Characterization and electrochemical measurements

The surface morphology and microstructure of the electrode materials were investigated using field emission scanning electron microscope (FESEM, Zeiss Ultra-Plus) and transmission electron microscopy (TEM, JEM-2100). Raman spectroscopy was performed using Raman spectrometer (Raman, Renishaw Invia Reflex System) in the range of 100-2000 cm^{-1}. This device was equipped with a He-Ne laser beam operating at a wavelength of 785 nm. Electrochemical analysis and measurements were carried out using an electrochemical workstation (CHI760C, CH Instruments) in a conventional three-electrode system with Pt sheet as a counter electrode, KCl-saturated calomel electrode as a reference electrode, CQDs-PPy/TiO_2 and PPy/TiO_2 nanotube hybrid as a working electrode. The cyclic voltammetry (CV) was conducted in 1 M H_2SO_4 electrolyte solution. The galvanostatic charge-discharge (GCD) measurements were performed in 1 M H_2SO_4 electrolyte solution under a controlled current density and potential window. Electrochemical impedance spectroscopy (EIS) measurements were implemented at 0.2 V vs SCE with ac-voltage amplitude of

5 mV over the frequency range of 0.01-100000 Hz after cyclic voltammetry tests in 1 M Na_2SO_4 electrolyte solution by using a electrochemical analyzer (IM6e ZAHNER Elektrik, Germany). The electrochemical measurement of flexible CQDs-PPy supercapacitor was conducted using a two-electrode testing system.

3. Results and discussion

3.1 Electrochemical deposition process

Fig. 1 shows the response current curves of CQDs-PPy/TiO_2 and PPy/TiO_2 nanotube hybrid during electropolymerization synthesis process. The current increment was insignificant when the initial electrode potential increased from 0.7 to 0.80 V. Actually, the electrochemical polymerization reaction of pyrrole monomer occurs predominately at an anodic potential above 0.8 V vs. SCE. The response current was very low in this initial reaction period below 0.8 V. A quick enhancement of response current could be then achieved when the electrode potential was further raised from 0.8 to 1.1 V. It indicates that ohmic resistance of as-formed CQDs-PPy/TiO_2 and PPy/TiO_2 gradually decreased along with continuous electrodeposition of PPy on TiO_2 nanotube array [16]. Comparatively, the response current was increased from $7.7*10^{-8}$ mA cm^{-2} for PPy/TiO_2 to $5.5*10^{-6}$ mA cm^{-2} for CQDs-PPy/TiO_2 at a critical potential of 0.7 V. The presence of CQDs in pyrrole monomer electrolyte could effectively promote the electropolymerization reaction, leading to forming highly conductive CQDs-PPy/TiO_2 electrode material.

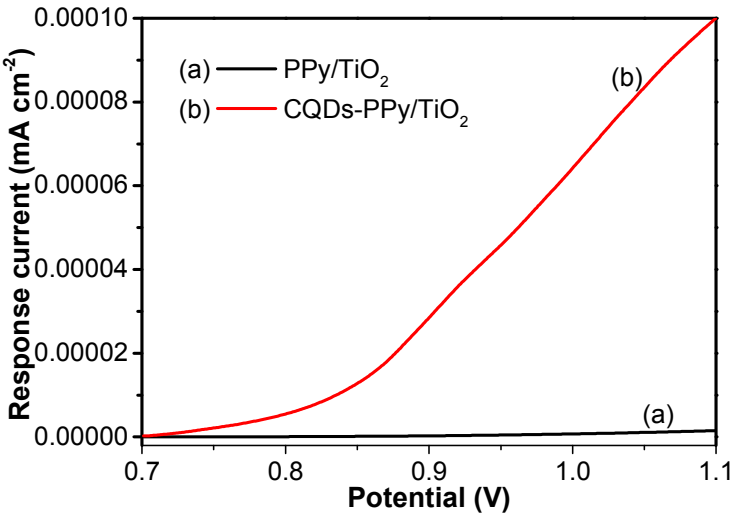

Fig. 1 Response current curves of (a) PPy/TiO_2 and (b) CQDs-PPy/TiO_2 nanotube hybrid in normal pulse voltammetry deposition process.

3.2 Microstructure characterization

TEM and SEM are employed to investigate morphologies and microstructures of CQDs and CQDs-PPy/TiO_2 nanotube hybrid. Fig. 2 (A) shows TEM images of the CQDs. It can be seen that the CQDs had a spherical shape and a narrow particle distribution of 3-7 nm. All CQDs were uniformally dispersed and seperated from each other without any aggregation. Fig. 2 (B) shows the UV-Vis absorption spectrum of CQDs. The appearance of maximum absorption wavelength at 235 nm was ascribed to the formation of CQDs [33, 34].

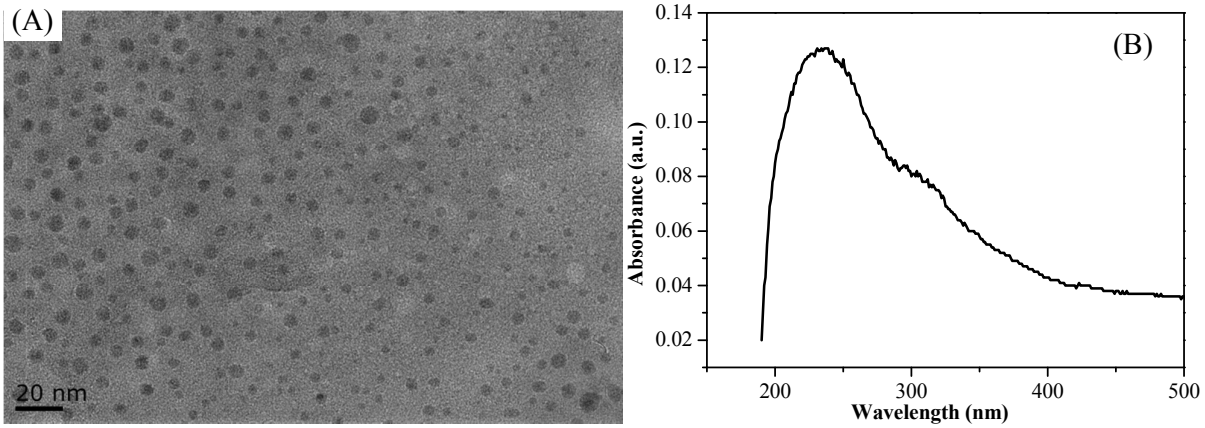

Fig. 2 (A) TEM image and (B) UV-Vis absorption spectrum of CQDs in aqueous solution.

Fig. 3 shows SEM images of TiO_2 nanotube array and CQDs-PPy/TiO_2 nanotube hybrid. TiO_2 had well-ordered and independent nanotube array structure with average inner diameter of 120-150 nm, the wall thickness of 10-20 nm and the total length of 1.1 μm (Fig. 3 A and B). CQDs-PPy/TiO_2 exhibited a highly-ordered heterogeneous coaxial nanotube structure and all these nanotube walls were inclined to bond together. It had average wall thickness of about 65-115 nm, the inner nanotube diameter of 35-90 nm. The total length of CQDs-PPy/TiO_2 was approximate 1.2 μm, which was close to or a little higher than the length of bare TiO_2 nanotubes. The ordered and coaxial CQDs-PPy/TiO_2 nanotube hybrid provided effective interface area to shorten ion diffusion path and electron transfer path, which was beneficial to form a good electrically conductive channel for supercapacitor application.

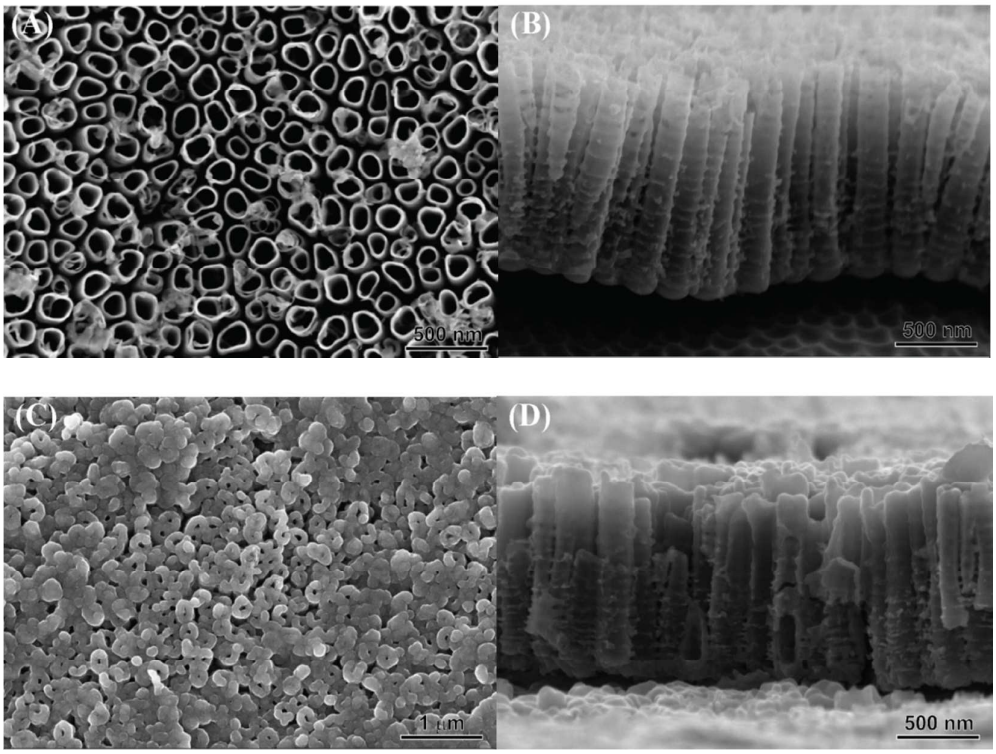

Fig. 3 SEM images of (A) top surface view and (B) cross-section view of TiO_2 nanotube array; (C) top surface view and (D) cross-section view of CQDs-PPy/TiO_2 nanotube hybrid.

3.2 Raman spectroscopy analysis

Raman spectroscopy measurement is used to confirm the formation of the as-prepared CQDs-PPy/TiO_2 nanotube hybrid. Fig. 4 shows the Raman spectra of CQDs, PPy and CQDs-PPy/TiO_2 in the range of 100-2000 cm^{-1}. Regarding CQDs, two characteristic Raman scattering peaks at 1376 and 1572 cm^{-1} were ascribed to the disordered D band and the ordered G band, respectively [35]. The broad peak at around 450 cm^{-1} was mostly ascribed to the substrate of as-anodized amorphous TiO_2 nanotube sheet, which was used to support CQDs. Considering PPy, Raman scattering peak at 1602 cm^{-1} was assigned to C=C stretching vibration. The peak at 1485 cm^{-1} was assigned to C–C stretching vibration. The peaks at 1396 cm^{-1} was assigned to C–N stretching vibration. The peak at 1245 cm^{-1} was caused by C–H in-plane bending vibration. The peaks at 1043 and 930 cm^{-1} were assigned to C–H ring deformation vibration [36, 37]. In view of CQDs-PPy/TiO_2 nanotube hybrid, Raman scattering peaks were mainly located at 1590, 1373 and 935 cm^{-1}. Comparatively, the characteristic Raman peaks of CQDs-PPy/TiO_2 nanotube hybrid were

very similar to those of CQDs and PPy. It proves that CQDs-PPy/TiO_2 nanotube hybrid included CQDs and PPy on the base of TiO_2 nanotube array through an electro-polymerization deposition process.

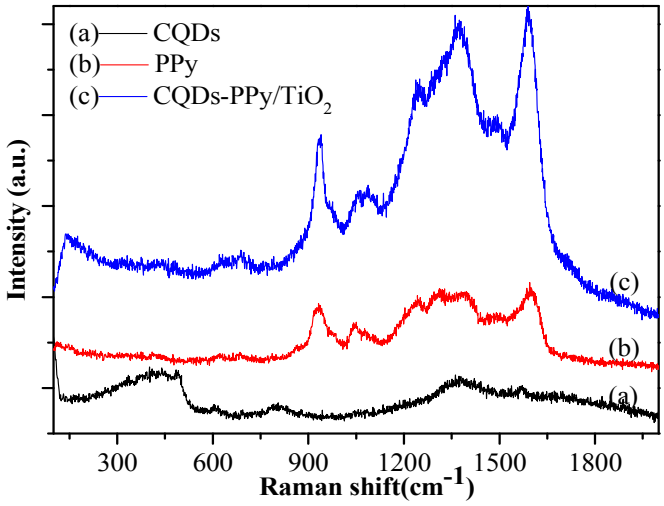

Fig. 4 Raman spectra of CQDs, PPy and CQDs-PPy/TiO_2 nanotube hybrid.

3.3 Electrochemical impedance spectroscopy analysis

Electrochemical impedance spectroscopy measurement is carried out to evaluate the charge transfer and ion diffusion properties of electrode materials. Fig. 5 shows Nyquist plots and equivalent circuit of CQDs-PPy/TiO_2 and PPy/TiO_2 nanotube hybrid at ac-voltage amplitude of 5 mV and requency range of 100 kHz-10 mHz in 1 M H_2SO_4 aqueous electrolyte. Nyquist plots of CQDs-PPy/TiO_2 and PPy/TiO_2 nanotube hybrid showed a small semicircle in high frequency region and a straight line along the imaginary axis in the low frequency region. The intersection of the curves at the real impedance axis in high-frequency region reflects total ohmic resistance (R_o), including resistance of electrolyte, intrinsic resistance of electrode material, and contact resistance at interface of electroactive material and current collector. The high-frequency impedance arc is attributed to the charge-transfer resistance (R_{ct}) between electroactive PPy and electrolyte in electrochemical process . The double layer capacitance (C_{dl}) attributes to the charge close to the porosity interface of nanotube hybrid. The Warburg element (W) represents the mass transport of reactants to and/or products from the electrode surface that may determine the electrochemical reaction rate of electroactive materials [38]. The constant phase elements (CPE) is used to account for the double layer

capacitance and pseudocapacitance. The pore resistance (R_{po}) represents the electron transfer resistance in the nanotube hybrid [39]. The detailed fitting results of equivalent circuit parameters are summarized in Table 1. R_o of CQDs-PPy/TiO_2 and PPy/TiO_2 nanotube hybrid was 0.154 and 0.817 Ω cm^{-2}, respectively. The coresponding R_{ct} was 0.00931 and 0.02241 Ω cm^{-2}, respectively. These results clearly demonstrate that CQDs improved electrical conductivity of CQDs-PPy/TiO_2 nanotube hybrid, resulting in higher charge transfer rate than PPy/TiO_2. C_{dl} was 0.248 and 0.579 mF cm^{-2} for CQDs-PPy/TiO_2 and PPy/TiO_2 nanotube hybrid, respectively. It indicateds that PPy/TiO_2 had more porosity interface than CQDs-PPy/TiO_2 due to partial nanotubes were fully covered by PPy. Warburg element represents the mass diffusion of reactant species in a finite or semi-infinite medium in low frequency region [40]. The corresponding Warburg impedance can be expressed by equation (1).

$$Z_W = \frac{\sigma}{\sqrt{\omega}} - j\frac{\sigma}{\sqrt{\omega}} \quad (1)$$

where σ is Warburg coefficient and ω is angular frequency ($\omega = 2\pi f$). W is defined by three values. W-R is the diffusion resistance and W-T is the diffusion time constant. W-P is a fractional exponent, which has a value near 0.5 with regard to the finite length diffusion characteristic [41]. In general, CPE in equivalent circuit in place of a capacitor is used to compensate for non-homogeneity in the system. CPE was related to the following factors such as inhomogeneity at electrode-electrolyte interface, porosity, nature of electrode, and dynamic disorder associated with diffusion [8]. CPE is defined by eqation (2).

$$CPE = \frac{1}{Q(j\omega)^n} \quad (2)$$

where Q is the frequency independent constant related to the surface and electrode substance, ω represents the angular frequency. n is a variable between 1 and 0, which is related to a non-uniform distribution due to roughness and/or the surface porosity. CPE shows different responses depending on this n value. n = 0 represents the pure resistance, whereas n = 1 represents the ideal capacitor response and n = 0.5 indicates Warburg impedance behavior. However, n > 0.5 represents moderate

capacitor behavior. Herein, n value was 0.999 and 0.962 for CQDs-PPy/TiO_2 and PPy/TiO_2 nanotube hybrid, respectively. It indicates that CQDs-PPy/TiO_2 nanotube hybrid performed better capacitor behavior. R_{po} was 17.9 and 115 Ω cm^{-2} for CQDs-PPy/TiO_2 and PPy/TiO_2 nanotube hybrid, respectively. R_o, R_{ct} and R_{po} values could be directly used to evaluate the electrical conductivity of electrode materials. CQDs modfication to PPy obviously improved its electrical conductivity, thus causing an effective pathway for charge transfer through electroactive PPy and leading to high capacitance performance of CQDs-PPy/TiO_2 nanotube hybrid.

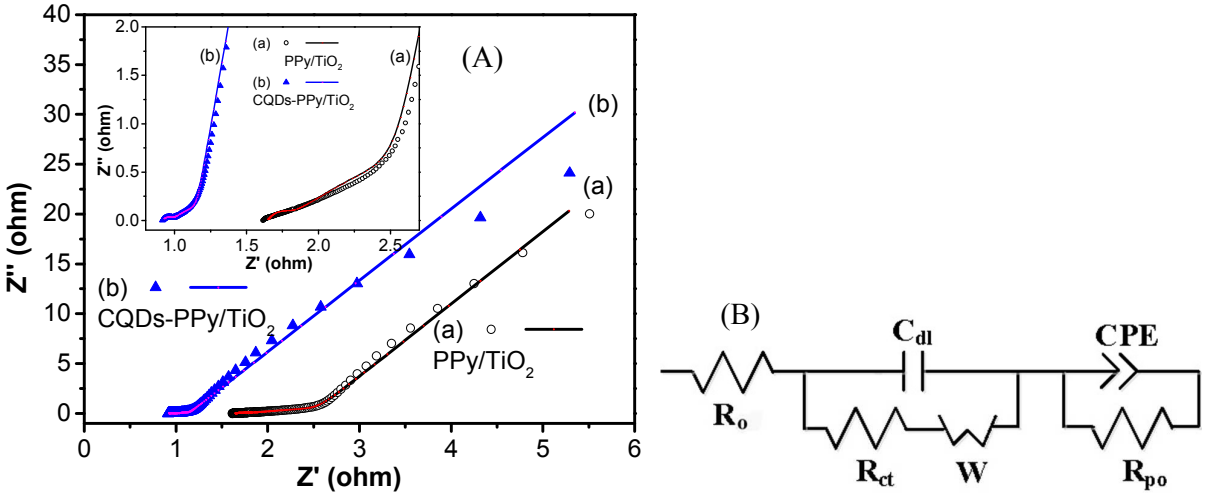

Fig. 5 (A) Nyquist plots and (B) equivalent circuit of CQDs-PPy/TiO_2 and PPy/TiO_2 nanotube hybrid in 1 M H_2SO_4 solution.

Table 1 Fitting values of equivalent circuit elements of CQDs-PPy/TiO_2 and PPy/TiO_2 nanotube hybrid.

Equivalent circuit elements	R_o (Ω m^{-2})	R_{ct} (Ω cm^{-2})	C_{dl} (mF cm^{-2})	CPE (S s^n cm^{-2})	n	R_{po} (Ω cm^{-2})	W-R (Ω cm^{-2})	W-T (s)	W-P
CQDs-PPy/TiO_2	0.154	0.00931	0.000248	0.633	0.999	17.9	0.098	0.452	0.434
CQDs-PPy	0.817	0.02241	0.000579	0.563	0.962	32.7	0.382	2.281	0.368

3.4 Cyclic voltametry analysis

Cyclic voltammetry measurement is carried out to evaluate the modification effect of CQDs on electrochemical performance of PPy. Fig. 6 (A) shows CV curves of CQDs-PPy/TiO_2 and PPy/TiO_2

nanotube hybrid at a scan rate of 20 mV s^{-1} in 1 M H_2SO_4 electrolyte solution with a potential range from -0.1 to 0.5 V. CV curves exhibited quasi-rectangular shape and near mirror-image symmetry with respect to the zero-current line, demonstrating a capacitive behavior. The current density and the enclosed area of CV curve of CQDs-PPy/TiO_2 nanotube hybrid was much larger than that of PPy/TiO_2, revealing higher electrical conductivity and capacitive performance. The specific capacitance is calculated using equation (3).

$$C_m = \frac{\int idv}{2m \times \Delta V \times v} \quad (3)$$

Where $\int idV$ is the integrated area of CV curves; m is the mass of electroactive material in the electrode; ΔV is the scanned potential window and v is the scan rate.

The calculated specific capacitance was increased from 241 F g^{-1} for PPy/TiO_2 to 440 F g^{-1} for CQDs-PPy/TiO_2 nanotube hybrid at a scan rate of 20 mV s^{-1}. The enhanced capacitance performance of CQDs-PPy/TiO_2 nanotube hybrid was attributed to the positive synergistic effect between CQDs and PPy. The incorporation of CQDs into PPy could provide conductive channel, rendering fast electron transfer in CQDs-PPy/TiO_2 nanotube hybrid [42].

Fig. 6 (B and C) shows CV curves of CQDs-PPy/TiO_2 and PPy/TiO_2 nanotube hybrid at different scan rates. When the scan rate increased from 5 to 200 mV s^{-1}, CV curve of CQDs-PPy/TiO_2 nanotube hybrid mostly kept a quasi-rectangular shape with small distortion, indicating good capacitive behavior for CQDs-PPy/TiO_2 nanotube hybrid. The proportionality of the peak current density with the scan rate implied that CQDs-PPy/TiO_2 nanotube hybrid had low ohmic resistance and good rate capabilities. Comparatively, CV curves of PPy/TiO_2 nanotube hybrid also exhibited quasi-rectangular shape at low scan rate from 5 to 50 mV s^{-1}, indicating its capacitive behavior. Nevertheless, due to the low conductivity of PPy/TiO_2, the shape of CV curves gradually deviated from typical rectangular shape when the scan rate was increased from 100 to 200 mV s^{-1}, presenting more resistor element properties involved in capacitor element. Fig. 7 (D) shows the specific capacitance of CQDs-PPy/TiO_2 and PPy/TiO_2 nanotube hybrid in terms of CV scan rate. The specific capacitance of CQDs-PPy/TiO_2 nanotube hybrid decreased from 529 to 251 F g^{-1}

when the scan rate increased from 5 to 200 mV s^{-1}, keeping 47.5% capacitance retention. Comparatively, the specific capacitance of PPy/TiO_2 nanotube hybrid dropped from 317 to 52 F g^{-1}, keeping only 16.4% capacitance retention. Accordingly, CQDs-PPy/TiO_2 performed higher capacitance and better rate capability than PPy/TiO_2.

The scan rate plays important role in the process of electron transfer and electrolyte ion diffusion into the electrode material. Generally, the specific capacitance decreased with the increase of scan rate. At low scan rate, electrolyte ion diffusion became sufficient towards external surface and inner active sites of electrode material. More complete redox reaction usually contributed to higher capacitance. At high scan rate, sufficient ion diffusion of electrolyte could delay the doping/dedoping process of PPy, resulting in a low capacitance. The inherent low electrical conductivity of bulk PPy caused high resistance for electron transfer. CQDs with superior electrical conductivity, number of carriers and charge carrier mobility paved the continuous electron transfer channels for CQDs-PPy/TiO_2 nanotube hybrid. The presence of CQDs in bulk PPy promoted electron transfer from PPy to current collector during electrochemical reaction process, which ultimately improved current density and specific capacitance [27].

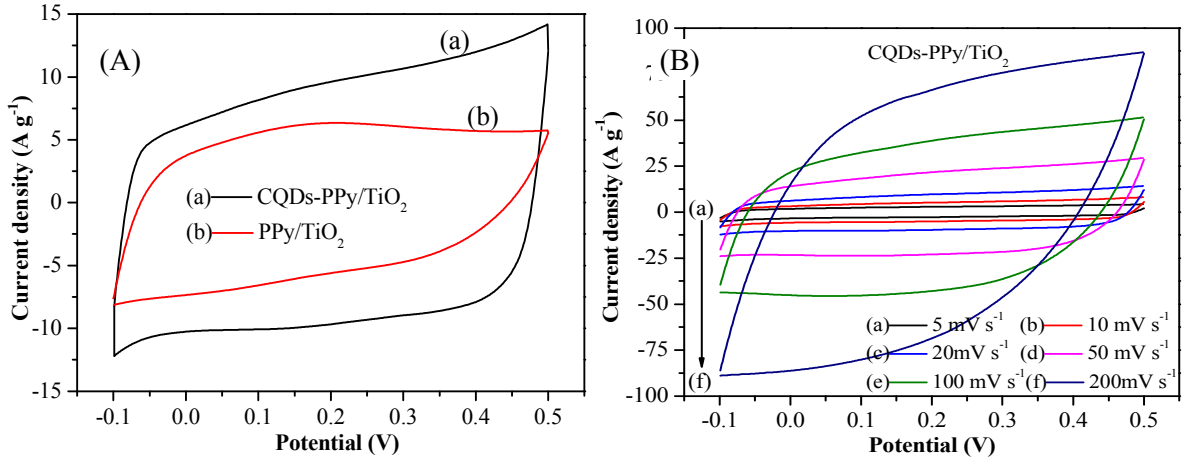

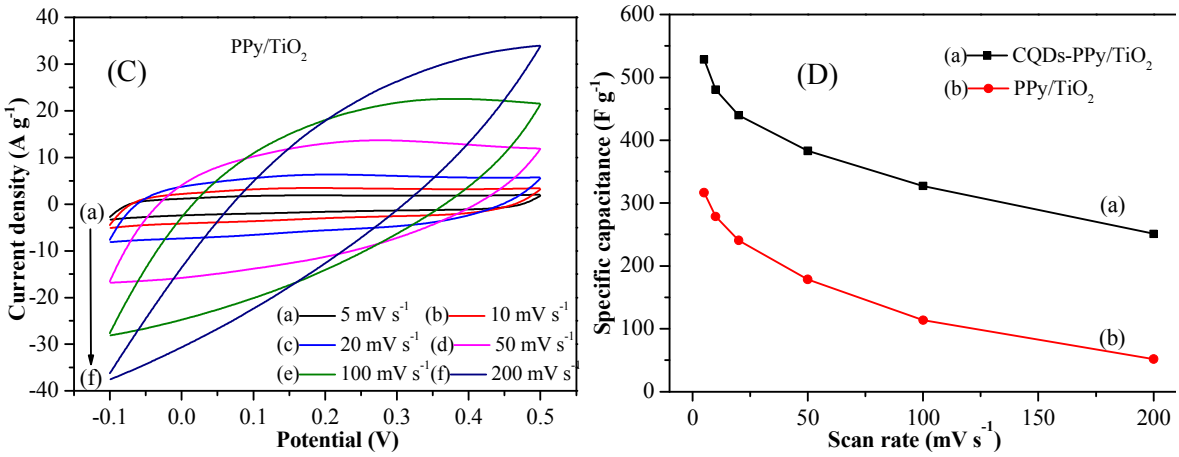

Fig. 6 (A) CV curves of CQDs-PPy/TiO_2 and PPy/TiO_2 nanotube hybrid in 1 M H_2SO_4 electrolyte solution at scan rate of 20 mV s^{-1}; CV curves of (B) CQDs-PPy/TiO_2 and (C) PPy/TiO_2 nanotube hybrid at different scan rates; (D) Corresponding specific capacitance in terms of CV scan rate.

3.5 Galvanostatic charge-discharge performance

Galvanostatic charge-discharge measurement is performed to further investigate electrochemical capacitance performance of CQDs-PPy/TiO_2 and PPy/TiO_2 nanotube hybrid electrodes. The specific capacitance is calculated using equation (4).

$$C_m = \frac{I \times \Delta t}{\Delta V \times m} \quad (4)$$

where C_m is the specific capacitance, I is the current of charge-discharge, Δt is the discharge time, ΔV is the scanned potential window, and m is the mass of active material in the electrode.

Fig. 7 (A) displays GCD curves of CQDs-PPy/TiO_2 and PPy/TiO_2 nanotube hybrid electrodes at a current density of 0.5 A g^{-1}. Both GCD curves exhibited the near triangle shapes, presenting a reversible and fast ion doping/dedoping PPy. The specific capacitance was increased from 482 F g^{-1} (or 161 mF cm^{-2}) for PPy/TiO_2 to 849 F g^{-1} (or 212 mF cm^{-2}) for CQDs-PPy/TiO_2. CQDs in the hybrid material served as a conductive path for electron shuttling during the charge-discharge process. CQDs-hybridized PPy decreased the electron transfer resistance and interficial contact resistance, which integratively promoted the electrochemical capacitance.

In addition, voltage drop across internal resistance (IR drop) was observed at initial discharge

curves. IR drop roughly reflects the internal resistance of electrode materials. It involves electronic resistance related to electroactive materials and ionic resistance related to electrolyte conductivity and ion mobility. IR drop was 2.1 mV and 16.8 mV for CQDs-PPy/TiO_2 and PPy/TiO_2 nanotube hybrid, demonstrating the superior electrical conductivity of CQDs-PPy/TiO_2. The negligibale IR drop of CQDs-PPy/TiO_2 nanotube hybrid indicated its high electrical conductivity of CQDs-PPy. Obvious IR drop of PPy/TiO_2 nanotube hybrid was ascribed to large internal resistance of PPy. Fig. 7 (B) shows GCD curves of CQDs-PPy/TiO_2 nanotube hybrid electrode at different current density from 0.5 to 5 A g^{-1}. At low current densities of 0.5 and 1 A g^{-1}, GCD curves were straight and had a very symmetric nature, suggesting a good reversibility and good coulombic efficiency during GCD processes. At higher current density from 1.5 and 5 A g^{-1} , a small IR drop was observed at initial discharge curves. But GCD curves were symmetric yet, indicating a reversible electrochemical behavior. The specific capacitance of CQDs-PPy/TiO_2 nanotube hybrid droped from 849 to 533 F g^{-1} (also 212 to 133 mF cm^{-2}) when the current density increased from 0.5 to 5 A g^{-1}, indicating a good capacitance retention of 62.8 %. Such capacitance was comparable to or even higher than the reported results. For instance, Dhibar et al. fabricated a silver-polyaniline/multiwalled carbon nanotubes nanocomposite and reported the highest specific capacitance of 528 F g^{-1} at 5 mV s^{-1} scan rate 1 M KCl solution [28]. Wei et al. deposited polypyrrole-silver composites on a nickel foam via the redox reaction between pyrrole and silver nitrate and reported the highest specific capacitance of 493 F g^{-1} in 0.5 M K_2SO_4 electrolyte at a current density of 1 A g^{-1} [29].

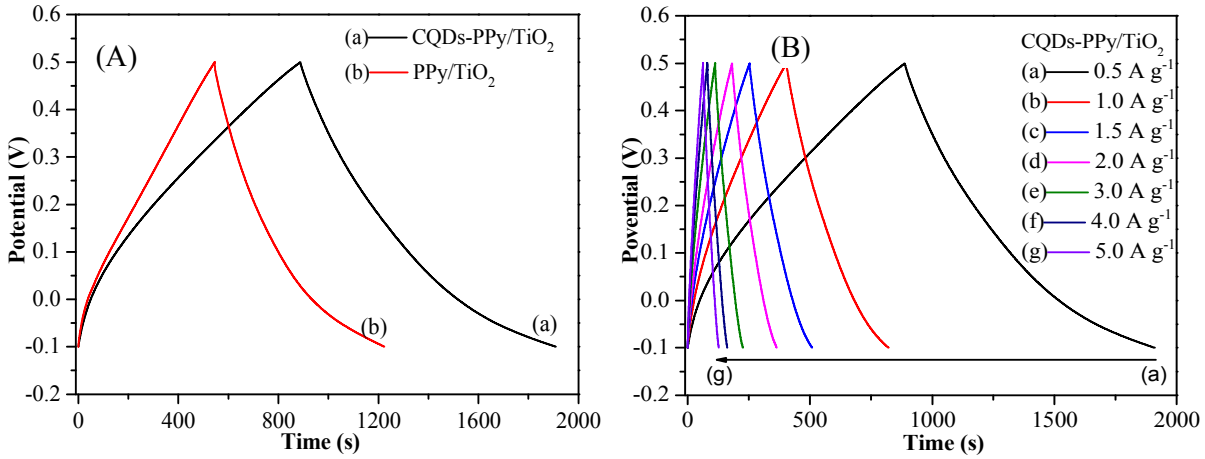

Fig. 7 (A) GCD curves of CQDs-PPy/TiO_2 and PPy/TiO_2 nanotube hybrid at 0.5 A g^{-1} in 1 M H_2SO_4 electrolyte solution; (B) GCD curves of CQDs-PPy/TiO_2 at current density of 0.5 - 5.0 A g^{-1}.

Good long-term cycle stability is required for supercapacitor application. Fig. 8 (A and B) show the cycling stability of CQDs-PPy/TiO_2 and PPy/TiO_2 nanotube hybrid at high current density of 20 A g^{-1} during 2000 cycles. The specific capacitance of CQDs-PPy/TiO_2 nanotube hybrid decreased from 317 to 283 F g^{-1} (also 79.3 to 70.8 mF cm^{-2}) , presenting 89.3% retention capacity. Comparatively, the specific capacitances of PPy/TiO_2 nanotube hybrid decreased from 107 to 84 F g^{-1} (also 35.7 to 28.1 mF cm^{-2}), presenting 78.5% retention capacity. The inserted image of Fig. 8 (A and B) reveals CQDs-PPy/TiO_2 and PPy/TiO_2 nanotube hybrid with 100 charge-discharge cycles at different current density. The capacitance decay of CQDs-PPy/TiO_2 nanotube hybrid at current density of 2, 4, 6, 8 and 10 A g^{-1} was 0.5%, 0.66%, 1%, 0.85% and 2.1%, respectively. Comparatively, the capacitance decay of PPy/TiO_2 nanotube hybrid at current density of 2, 4, 6, 8 and 10 A g^{-1} was 1%, 2.5%, 2.3%, 1.1% and 2.8%, respectively. CQDs-PPy/TiO_2 nanotube hybrid exhibited better rate capability a bit. Usually, PPy-based electrode material usually sufers from poor cycling stability because the swelling and shrinking of PPy could lead to polymer degradation. However, CQDs-PPy/TiO_2 exhibited good cycling stability when CQDs was incorporated into PPy. CQDs provided a robust support for PPy, thus enhancing the mechanical strength and preventing PPy from severely swelling and shrinking during cycling charge-discharge process. Therefore, CQDs-PPy/TiO_2 nanotube hybrid exhibited a better stability than PPy/TiO_2 nanotube hybrid.

In addition, the energy density and the power density are also important parameters to evaluate energy stroage of supercapacitor electrode materials. They can be calculated using the following equation (5) and (6).

$$E = \frac{I \times \Delta V \times \Delta t}{2m} = \frac{1}{2} \times C \times \Delta V^2 \quad (5)$$

$$P = \frac{I \times \Delta V}{2m} \quad (6)$$

where E is the energy density, P is the power density, I is the current of charge-discharge, Δt is the discharge time, ΔV is the scanned potential window, and m is the mass of active material in the electrode.

Fig. 8 (C) shows the Ragone plot (power density vs. energy density) of CQDs-PPy/TiO_2 nanotube hybrid calculated from GCD curves. CQDs-PPy/TiO_2 nanotube hybrid exhibited an energy density of 42.5 W h kg^{-1} at a power density of 150 W kg^{-1}, while it still maintained 26.5 W h kg^{-1} at high power density of 1500 W kg^{-1}. CQDs-PPy/TiO_2 nanotube hybrid electrode with high energy density suggested its unique capability to meet the requirement for high capacitance and long cycling life. The uniform ordered structure of CQDs-PPy nanohybrid provided a highly accessible electrochemically surface for ultilizing full active site of PPy. The effective incorporation CQDs into PPy could simultaneously increase electrochemical capacitance and cycle stability of PPy, leading to a superior electrochemical performance.

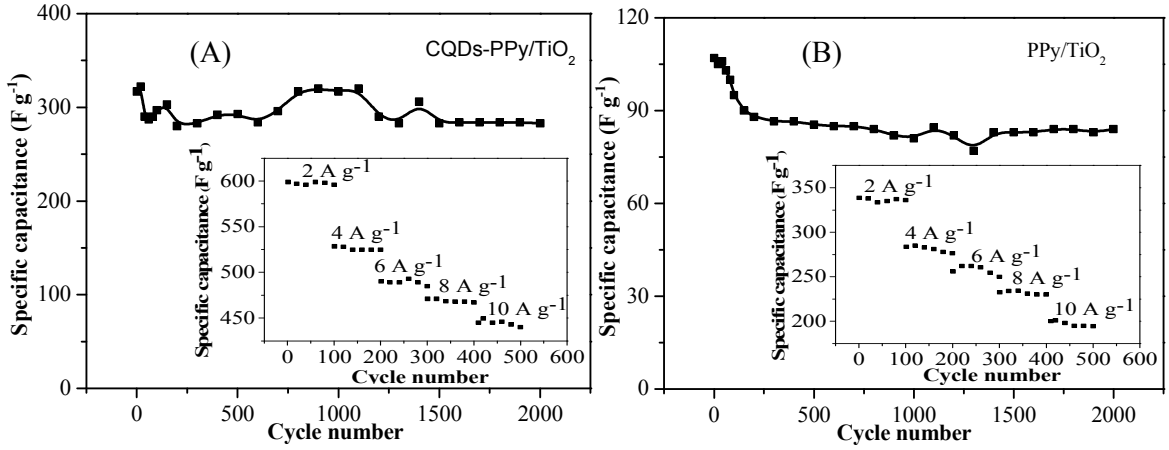

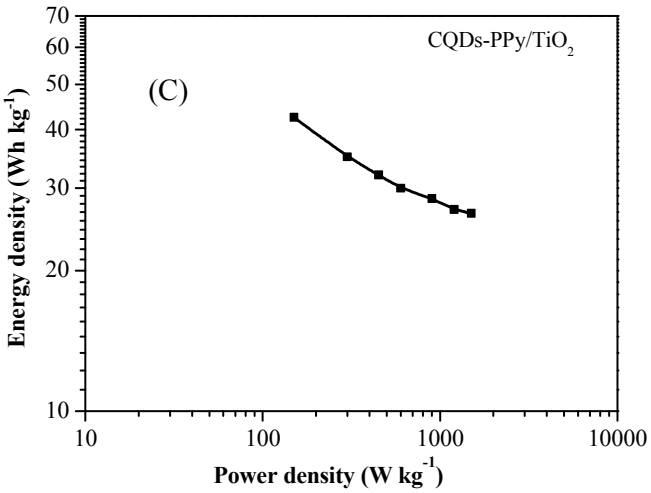

Fig. 8 (A, B) Galvanostatic charge–discharge cycling stability of CQDs-PPy/TiO_2 and PPy/TiO_2 nanotube hybrid at a current density of 20 A g^{-1} during 2000 cycles; (C) Ragone plots of CQDs-PPy/TiO_2 nanotube hybrid.

3.6 Flexible all-solid-state supercapacitor

Flexible solid-state supercapacitor was also investigated using CQDs-PPy nanohybrid which was fabricated by removing TiO_2 template from CQDs-PPy/TiO_2. Fig. 9 shows photographs of flexible CQDs-PPy supercapacitor in planar state and bending state. As-fabricated CQDs-PPy supercapacitor had total area of 13 cm× 30 mm and total thickness of 0.6 mm. The supercapacitor could be fully folded by 180° to achieve stable charge-discharge process, demostrating good flexibility of this supercapacitor.

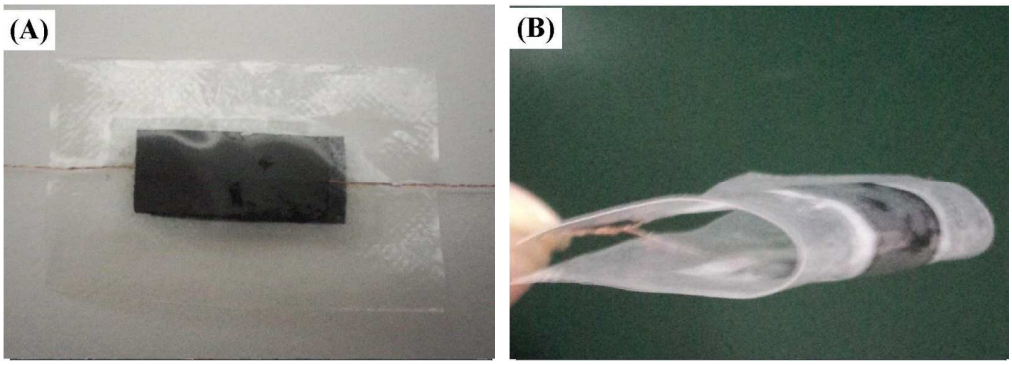

Fig. 9 Photographs of flexible CQDs-PPy supercapacitor in (A) planar state and (B) bending state.

The electrochemical performance of CQDs-PPy supercapacitor was also investigated. Fig. 10

(A) shows CV curves of CQDs-PPy supercapacitor at a scan rate of 20 mV s^{-1} when this supercapacitor keeps at a planar state and bending state. CQDs-PPy supercapacitor exhibited the similar capacitance performance by comparing the integral areas of CV curves. The corresponding specific capacitance was estimated to be 5.92 and 6.09 F g^{-1}, confirming an excellent mechanical stability and flexibility of this CQDs-PPy supercapacitor. Fig. 10 (B) shows CV curves of CQDs-PPy supercapacitor at different current density. The shape of CV curves was indicative of the characteristic supercapacitor behavior. The specific capacitance decreased from 20 to 1.1 F g^{-1} when the scan rate was increased from 5 to 200 mV s^{-1}. Such a capacitance decrease along with increasing scan rate was attributed to the reason that the inner active sites in the gel electrolyte could not sustain fast redox transition at high scan rates.

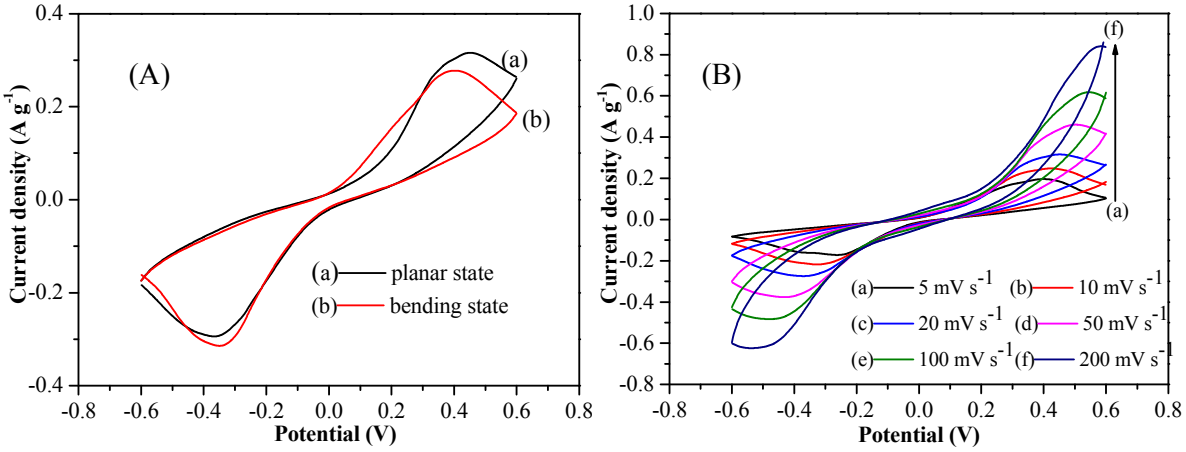

Fig. 10 CV curves of flexible CQDs-PPy supercapacitor (A) at a planar state and bending state, (B) at different scan rate.

Fig. 11 displays GCD curve of flexible CQDs-PPy supercapacitor in a potential window from -0.6 to 0.6 V. The shape of GCD curve indicated the dominating contribution of pseudocapacitance. Obvious IR drop revealed the larger ohmic internal resistance using gel electrolyte rather than aqueous electrlyte. On the other hand, the potential window of CQDs-PPy all-solid-state supercapacitor had been obviously increased. The specific capacitances of CQDs-PPy supercapacitor was 14.5 F g^{-1} at a current density of 0.02 A g^{-1}. This flexible CQDs-PPy supercapacitor exhibited much higher capacitance than our previously reported flexible PPy

supercapacitor which was 13 F g^{-1} at low current density of 0.005 A g^{-1} [9]. It demonstrates high possibility for this CQDs-PPy supercapacitor to be used as flexible electronic devices in future.

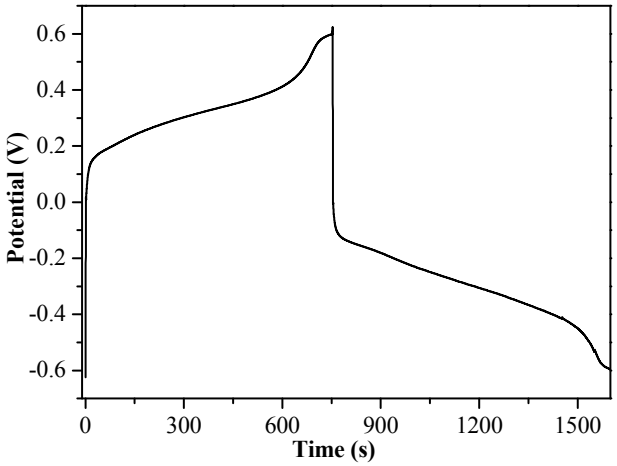

Fig. 11 GCD curve of flexible CQDs-PPy supercapacitor at a current density of 0.02 A g^{-1}.

4. Conclusions

CQDs-PPy/TiO_2 nanotube hybrid was fabricated as supercapacitor electrode material by the controlled electrochemical synthesis route. CQDs-PPy/TiO_2 nanotube hybrid presented a highly ordered and heterogeneous coaxial nanotube structure. CQDs hybridizing modification could well improve the electrical conductivity of PPy. The charge transfer resistance decreased from 22.4 mΩ cm^{-2} to 9.3 mΩ cm^{-2} and the ohmic resistance decreased from 0.817 for to 0.154 Ω cm^{-2} when PPy/TiO_2 was converted into CQDs-PPy/TiO_2 nanotube hybrid. The specific capacitance was promoted from 482 F g^{-1} (or 161 mF cm^{-2}) for PPy/TiO_2 to 849 F g^{-1} (or 212 mF cm^{-2}) for CQDs-PPy/TiO_2 in 1.0 M H_2SO_4 electrolyte solution at a current density of 0.5 A g^{-1}. The capacitance retention was slightly increased from 78.5% to 89.3% after 2000 cycles at high current density of 20 A g^{-1}. The flexible all-solid-state supercapacitor based on CQDs-PPy nanohybrid electrode and PVA/H_2SO_4 gel electrolyte exhibited specific capacitance of 14.5 F g^{-1} at a current density of 0.02 A g^{-1} and stable capacitive performance at planar and bending state. The effective incorporation CQDs into PPy could simultaneously increase electrochemical capacitance and cycle stability of PPy, leading to a superior electrochemical performance. CQDs-hybridized PPy

presented the promising application as supercapacitor electrode material for energy storage.

Acknowledgements

The work was supported by National Natural Science Foundation of China (No. 21373047 and 20871029), Program for New Century Excellent Talents in University of the State Ministry of Education (No. NCET-08-0119), Science & Technology Program of Suzhou City (No. ZXG2012026, SYN201208, SYG201017).

Notes and references

1. Y. J. Peng, T. H. Wu, C. T. Hsu, S. M. Li, M. G. Chen and C. C. Hu, *J. Power Sources*, 2014, **272**, 970.
2. H. Mudila, V. Joshi, S. Rana, M. G. H. Zaidi and S. Alam, *Carbon Letters*, 2014, **15**, 171.
3. Y. Xie, H. Du and C. Xia, *Microporous Mesoporous Mater.*, 2015, **204**, 163.
4. Y. Xie, C. Xia, H. Du and W. Wang, *J. Power Sources*, 2015, **286**, 561.
5. C. Xia, Y. Xie, H. Du and W. Wang, *J. Nanopart. Res.*, 2015, DOI: 10.1007/s11051.
6. C. Xia, Y. Xie, W. Wang and H. Du, *Synth. Met.*, 2014, **192**, 93.
7. W. H. Sun, Z. L. Mo, H. L. Li, Y. Sun and Y. Q. Zhou, *Polym. Eng. Sci.*, 2014, **54**, 2731.
8. H. Du, Y. Xie, C. Xia, W. Wang and F. Tian, *New J. Chem.*, 2014, **38**, 1284.
9. H. Du, Y. Xie, C. Xia, W. Wang, F. Tian and Y. Zhou, *Mater. Lett.*, 2014, **132**, 417.
10. Y. Xie, D. Wang, Y. Zhou, H. Du and C. Xia, *Synth. Met.*, 2014, **198**, 59.
11. S. B. Ye and J. C. Feng, *Acs Appl. Mater. Interface*, 2014, **6**, 9671.
12. Y. Xie and Y. Zhan, *J. Porous Mater.*, 2015, **22**, 403.
13. A. H. P. de Oliveira and H. P. de Oliveira, *J. Power Sources*, 2014, **268**, 45.
14. Y. Xie and W. Wang, *J. Chem. Technol. Biotechnol.*, 2015, DOI: 10.1002/jctb.4737.
15. W. Wang, Y. Xie, Y. Wang, H. Du, C. Xia and F. Tian, *Microchim. Acta*, 2014, **181**, 381.
16. Y. Xie and H. Du, *J. Solid State Electrochem.*, 2012, **16**, 2683.
17. W. Khoh and J. Hong, *Colloids Surf. Physicochem. Eng. Aspects*, 2014, **456**, 26.
18. Y. Xie and X. Fang, *Electrochim. Acta*, 2014, **120**, 273.
19. F. Tian, Y. Xie, H. Du, Y. Zhou, C. Xia and W. Wang, *RSC Adv.*, 2014, **4**, 41856.
20. Y. Xie, F. Song, C. Xia and H. Du, *New J. Chem.*, 2015, **39**, 604.
21. Y. Xie, Y. Wang and H. Du, *Mater. Sci. Eng., B*, 2013, **178**, 1443.

22. K. B. Xu, X. J. Huang, Q. Liu, R. J. Zou, W. Y. Li, X. J. Liu, S. J. Li, J. M. Yang and J. Q. Hu, *J. Mater. Chem. A*, 2014, **2**, 16731.

23. H. H. Zhou, G. Y. Han, Y. M. Xiao, Y. Z. Chang and H. J. Zhai, *J. Power Sources*, 2014, **263**, 259.

24. Y. Xie and Y. Meng, *RSC Adv.*, 2014, **4**, 41734.

25. Y. Xie, Y. Jin, Y. Zhou and Y. Wang, *Appl. Surf. Sci.*, 2014, **313**, 549.

26. W. Wang, Y. Xie, C. Xia, H. Du and F. Tian, *Microchim. Acta*, 2014, **181**, 1325.

27. D. S. Patil, S. A. Pawar, R. S. Devan, M. G. Gang, Y. R. Ma, J. H. Kim and P. S. Patil, *Electrochim. Acta*, 2013, **105**, 569.

28. S. Dhibar and C. K. Das, *Ind. Eng. Chem. Res.*, 2014, **53**, 3495.

29. J. T. Wei, G. Z. Xing, L. Gao, H. Suo, X. P. He, C. Zhao, S. Li and S. X. Xing, *New J. Chem.*, 2013, **37**, 337.

30. S. Chen and I. Zhitomirsky, *Mater. Lett.*, 2014, **135**, 47.

31. X. Wu, X. Hong, Z. Luo, K. S. Hui, H. Chen, J. Wu, K. N. Hui, L. Li, J. Nan and Q. Zhang, *Electrochim. Acta*, 2013, **89**, 400.

32. B. Andres, S. Forsberg, A. Paola Vilches, R. Zhang, H. Andersson, M. Hummelgård, J. Bäckström and H. Olin, *Nord. Pulp Pap. Res. J.*, 2012, **27**, 481.

33. X. F. Chen, W. X. Zhang, Q. J. Wang and J. Y. Fan, *Carbon*, 2014, **79**, 165.

34. Q. L. Zhao, Z. L. Zhang, B. H. Huang, J. Peng, M. Zhang and D. W. Pang, *Chem. Commun.*, 2008, 5116.

35. L. Wang, Y. L. Wang, T. Xu, H. B. Liao, C. J. Yao, Y. Liu, Z. Li, Z. W. Chen, D. Y. Pan, L. T. Sun and M. H. Wu, *Nat. Commun.*, 2014, **5**.

36. Y. K. Lee, K. J. Lee, D. S. Kim, D. J. Lee and J. Y. Kim, *Synth. Met.*, 2010, **160**, 814.

37. S. Bose, T. Kuila, M. E. Uddin, N. H. Kim, A. K. T. Lau and J. H. Lee, *Polym.*, 2010, **51**, 5921.

38. A. M. Dhirde, N. V. Dale, H. Salehfar, M. D. Mann and T. H. Han, *IEEE Trans. Energy Conversion*, 2010, **25**, 778.

39. R. F. Li, Z. G. Li, Y. Y. Zhu and K. Qi, *J. Alloys Compd.*, 2013, **580**, 327.

40. W. J. Kuang, J. A. Mathews, M. L. Taylor and D. D. Macdonald, *Electrochim. Acta*, 2014, **136**, 493.

41. C. Xia, Y. Xie, Y. Wang, W. Wang, H. Du and F. Tian, *J. Appl. Electrochem.*, 2013, **43**, 1225.

42. Y. S. Lim, Y. P. Tan, H. N. Lim, N. M. Huang, W. T. Tan, M. A. Yarmo and C. Y. Yin, *Ceram. Int.*, 2014, **40**, 3855.